

Modulate and Reconstruct: Learning Hyperspectral Imaging from Misaligned Smartphone Views

Daniil Reutsky¹, Daniil Vladimirov^{2,3}, Yasin Mamedov^{2,3},
Georgy Perevozchikov¹, Nancy Mehta¹, Egor Ershov^{2,3,4}, and
Radu Timofte¹

¹JMU, Würzburg

²CRSI, Moscow

³MIRIAI, Moscow

⁴AXXX, Moscow

Abstract

Hyperspectral reconstruction (HSR) from RGB images is a highly promising direction for accurate color reproduction and material color measurement. While most existing approaches rely on a single RGB image — thereby limiting reconstruction accuracy — the majority of modern smartphones are equipped with two or more cameras. In this work, we propose a novel multi-image-to-hyperspectral reconstruction (MI-HSR) framework that leverages a triple-camera smartphone system, where two lenses are equipped with carefully selected spectral filters. Our easy-to-implement configuration, based on theoretical and empirical analysis, allows to obtain more complete and diverse spectral data than traditional single-chamber setups. To support this new paradigm, we introduce Doomer, the first dataset for MI-HSR, comprising aligned images from three smartphone cameras and a hyperspectral reference camera across diverse scenes. We further introduce a lightweight alignment module for MI-HSR that effectively fuses multi-view inputs while mitigating parallax- and occlusion-induced artifacts. Proposed module demonstrate consistent quality improvements for modern HSR methods. In a nutshell, our setup allows 30% more accurate estimations of spectra compared to an ordinary RGB camera, while the proposed alignment module boosts the reconstruction quality of SotA methods by an additional 5%. Our findings suggest that spectral filtering of multiple views with commodity hardware unlocks more accurate and practical hyperspectral imaging.

1 Introduction

Hyperspectral imaging provides dense spectral measurements at each spatial pixel, forming a 3D cube $\mathbf{Y} \in \mathbb{R}^{h \times w \times n}$, where $n \gg 3$. This enables fine-grained analysis

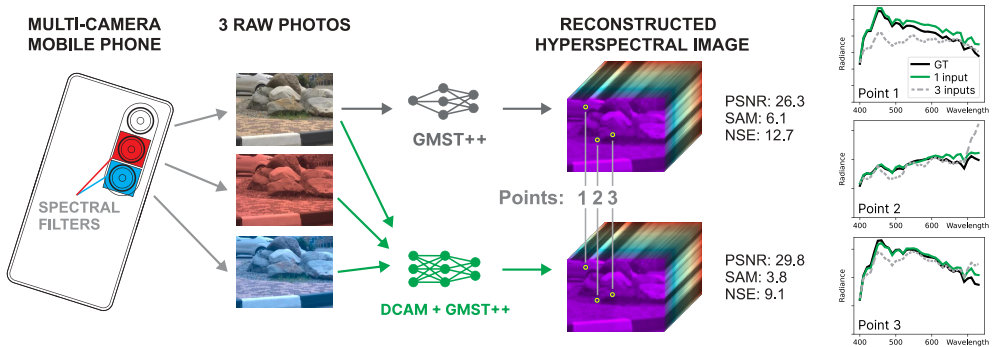


Figure 1: Proposed low-cost mobile spectral imaging system that transforms a standard smartphone into a spectrally diverse capture device via external filters on auxiliary cameras. This configuration enables simultaneous, multi-channel acquisition without internal hardware modification, supporting practical and scalable hyperspectral reconstruction.

of material properties in applications ranging from remote sensing [1], to medical diagnostics [2], to historical preservation [3], to ISP improvement [4, 5], to food quality assessment [6, 7]. However, acquiring such high-dimensional data typically requires hardware that is expensive, bulky, and often reliant on time-consuming scanning thus fundamentally limiting the usability of hyperspectral imaging in dynamic or consumer settings.

An increasingly studied alternative is *hyperspectral reconstruction* (HSR): recovering \mathbf{Y} from an RGB observation $\mathbf{X} \in \mathbb{R}^{h \times w \times 3}$ captured via a sensor with a spectral sensitivity matrix $\mathbf{C} \in \mathbb{R}^{3 \times n}$ under noise realization \mathbf{N} :

$$\mathbf{X} = \mathbf{Y}\mathbf{C} + \mathbf{N}.$$

This inverse problem is highly ill-posed and despite advances in deep learning-based HSR [8, 9], reconstructing \mathbf{Y} from a single RGB view remains fundamentally limited by the low spectral observability.

Several efforts have aimed to improve this observability. Learned or optimized multispectral filter arrays (MSFAs) [10], end-to-end spectral sensitivity learning [11], and joint sensor-network co-design [12] have all been proposed. However, these methods assume control over sensor hardware and manufacturing, thus making them impractical for scalable or consumer-level deployment.

One underexplored but promising path is to leverage the multi-camera systems found in modern smartphones. These devices already include multiple rear cameras with different lenses and spectral sensitivities. In principle, such a setup can be treated as a low-cost, multi-spectral capture system thus capable of observing a scene through multiple, distinct sensitivity matrices. However, prior works on leveraging multiple cameras [13, 14] do not tackle unavoidable image misalignment.

Can we turn a multi-camera smartphone into a compact, spectrally diverse imaging system, without altering its internal hardware? Our key insight is that by modulating the spectral response of the auxiliary cameras using carefully chosen external filters,

we can create an imaging system that allows richer spectral representations. Unlike synthetic MSFAs or custom hardware, our approach requires no internal modification and enables real-time, parallel acquisition. Critically, this setup is easy to deploy, manufacturable at scale, and compatible with existing mobile infrastructure.

We select filters using spectral information loss minimization with respect to a prior hyperspectral distribution. The resulting setup produces spatially misaligned but spectrally rich multi-view data thus posing a new fusion problem that we address via alignment-aware learning. An overview of our physical configuration is shown in Fig. 1, which illustrates how external filters are applied to the auxiliary lenses of a standard smartphone to create a spectrally diverse input set. The combination of low-cost physical augmentation and learning-based reconstruction represents a practical path toward deployable hyperspectral imaging in unconstrained environments. We propose a complete, low-cost pipeline for *multi-image-to-hyperspectral reconstruction (MI-HSR)* using a filter-modified smartphone. Specifically, the contributions are three-fold:

- A novel, low-cost spectral acquisition system that converts a commodity triple-camera smartphone into a 9-channel imaging device. This is achieved by augmenting the auxiliary cameras with two external spectral filters, which are theoretically selected using a spectral uncertainty minimization criterion to maximize captured information.
- A novel framework for multi-image hyperspectral reconstruction (MI-HSR), featuring our novel alignment-aware block. It fuses spatially misaligned and spectrally diverse inputs by leveraging optical-flow-guided deformable convolutions. Such utilization of auxiliary inputs allows +2.44 dB PSNR improvement over single-image HSR.
- The Doomer dataset, the first real-world benchmark for the MI-HSR task. The dataset contains 155 real-world scenes, each providing spatially misaligned RAW images from the filtered smartphone setup and a corresponding ground-truth hyperspectral scan.

2 Related Work

Low-cost multispectral imaging Numerous approaches have aimed to capture multispectral or hyperspectral information without expensive hardware. Early work by Helling et al. [20] employed a grayscale camera with a rotating filter wheel, while Valero et al. [21] used an RGB camera with three interchangeable filters. Oh et al. [14] captured scenes with three different cameras, leveraging the variation in their spectral sensitivities. More recently, Sharma et al. [13] demonstrated that consumer mobile devices with both RGB and NIR sensors can achieve extended spectral capture (400–1000 nm). Although these systems reduce costs, they either involve long capture times or assume no misalignment between successive captures.

Hyperspectral reconstruction from RGB Traditional HSR methods model spectra using sparse coding [17], dictionary learning [22], or manifold embeddings [23], based

Dataset	# scenes	Spectral data	Color reference	Spectral sampling Range (step), nm	Corresponding RGBs
CAVE [15]	32	Reflectance	Color chart or no	400–700 (10)	simulated BMP
Harvard [16]	79	Radiance	No	400–720 (10)	No
ICVL [17]	200	Radiance	Color chart or no	400–1000 (10)	simulated JPEG
KAUST [18]	409	Reflectance	White patch	400–730 (10)	No
Arad 1K [19]	949	Radiance	No	400–700 (10)	simulated JPEG
Beyond RGB [5]	1680	Radiance	Color chart	380–730 (20)	2× real RAW
MobileSpec [4]	200	Radiance	No	400–1000 (10)	real RAW
Doomer	155	Radiance	Gray ball	400–730 (10)	3× real RAW

Table 1: Overview of existing datasets for HSR from RGB. Our proposed Doomer dataset uniquely offers real multi-view RGB images with spectral filters, misalignment, and in-scene gray reference under diverse conditions.

on the low-dimensional structure of hyperspectral data and the rarity of metamers [24]. These approaches are computationally efficient but often lack the capacity to incorporate global context from the input image, making them less robust to complex natural scenes. Recent methods based on deep learning have achieved significant advances, particularly those developed through the NTIRE spectral reconstruction challenges [19]. Early deep models used CNNs [25, 26], while newer transformer-based approaches like MST++ [8] and SPECAT [27] introduced attention along spectral or spatial dimensions, and diffusion based approaches like SDM [28] or LDERT [29] also adapted for HSR. However, nearly all research relies on synthetic RGB inputs rendered from hyperspectral images (HSIs) using color matching functions (CMFs), assuming perfect alignment and sometimes access to camera parameters. These assumptions do not hold in practice, limiting model generalizability and non-sustainable to hard metameric cases [30, 28]. We address these limitations training and evaluating on real-world data with acquisition artifacts and misalignments.

Hyperspectral datasets Early datasets like CAVE [15] and Harvard [16] provided controlled hyperspectral measurements. Later datasets such as ICVL [17], KAUST [18], and Arad 1K [19] focused on enabling data-driven HSR methods. These datasets contain either radiance or reflectance data, but most lack real RGB images and instead simulate RGB via given sensor spectral sensitivities, which fails to capture the characteristics of camera pipelines. Moreover, they often assume perfect alignment, which does not hold in practical settings. Recent datasets like BeyondRGB [5] and MobileSpec [4] address some of these issues by including real RGB captures. BeyondRGB includes color charts and light source spectrum estimation, while MobileSpec offers aligned RGB-HSI pairs. However, they still face trade-offs between alignment, diversity, and color reference availability. We build on these efforts by introducing Doomer dataset with real misaligned RGB images, hyperspectral data, and in-scene color references thus enabling realistic reconstruction under natural capture conditions.

Handling misalignment Misalignment between inputs is a well-known challenge in video and reference-based super-resolution tasks. Optical flow (OF) [31, 32], deformable

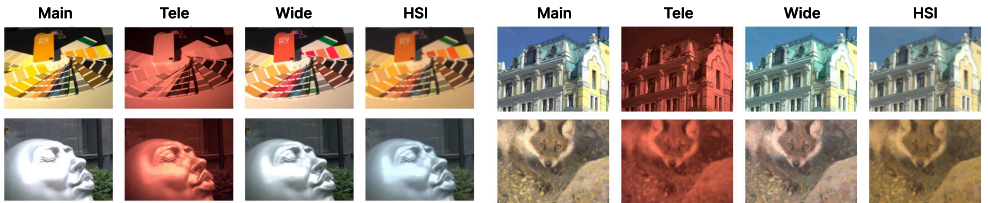


Figure 2: Sample scenes from the Doomer dataset. Smartphone images are rendered to sRGB using color matrices from RAW metadata; hyperspectral images are rendered using CIE RGB color matching functions.

convolutions [33, 34], attention mechanisms [35] have been proposed to mitigate this. In our context, misalignment also arises due to ground truth HSIs being not spatially aligned with the RGB input. Zhang et al. [36] addressed this by warping ground truth toward the input using OF, enabling pixel-level evaluation. Elezabi et al. [37] proposed contextual losses and pseudo-aligned inputs as training strategies. We adopt the interpretable and evaluation-friendly approach [36] of warping the ground truth to the input using OF, allowing accurate pixel-wise supervision and metric computation.

3 Proposed Imaging System

3.1 System Overview

To amplify spectral diversity, we cover Tele- and Wide cameras with external filters. As illustrated in Fig. 1, this converts each RGB camera into a spectrally modulated sensor. The resulting device captures nine distinct spectral channels without requiring scanning or hardware changes.

Formally, let $\mathbf{C}_i \in \mathbb{R}^{3 \times n}$ be the spectral sensitivity functions (SSF) of camera i , and $\mathbf{f}_i \in [0, 1]^n$ the spectral transmittance of the filter applied to that camera. Thus, per-camera response becomes $\mathbf{C}_i \odot \mathbf{f}_i$, and the overall response is:

$$\mathbf{C}_F = [(\mathbf{C}_0 \odot \mathbf{f}_0)^\top; \dots; (\mathbf{C}_{k-1} \odot \mathbf{f}_{k-1})^\top]^\top \in \mathbb{R}^{3k \times n},$$

where $\mathbf{F} = [\mathbf{f}_0^\top; \dots; \mathbf{f}_{k-1}^\top]$ is the filter configuration and \odot is element-wise multiplication. In our prototype, $k = 3$, with one unfiltered camera ($\mathbf{f}_0 = (1, \dots, 1)^\top$) and two filtered cameras. This design simplifies dataset collection (Sec. 4) while still significantly enriching spectral representations.

This configuration has two practical advantages. First, all channels are captured simultaneously under natural illumination, making it suitable for dynamic scenes. Second, it relies entirely on off-the-shelf hardware components. However, as each camera has a distinct physical position, the resulting images are spatially misaligned. This necessitates learning-based alignment modules, which we incorporate into our reconstruction pipeline (Sec. 5).

3.2 Filter Selection via Spectral Uncertainty Minimization

The effectiveness of our imaging system critically depends on the choice of spectral filters. Since we train on fully real-world data, the filter configuration must be fixed prior to data collection.

Given a library of 65 candidate filters from standard set, we exhaustively evaluate all 65×64 ordered filter pairs for the two auxiliary cameras. The optimal pair should minimize spectral ambiguity — i.e., the uncertainty in the latent spectrum $\mathbf{y} \in \mathbb{R}^n$ given a measurement $\mathbf{x} = \mathbf{C}_F \mathbf{y} + \mathbf{n}$, where \mathbf{n} is sensor noise.

Following [38], we use the expected conditional variance of the spectrum as a selection criterion:

$$v(\mathbf{F}) = \mathbb{E}_{\mathbf{x}} [\text{tr Var}_{\mathbf{y}}(\mathbf{y} \mid \mathbf{x})].$$

This criterion reflects the average spectral uncertainty remaining after observing \mathbf{x} . Lower $v(\mathbf{F})$ implies more informative measurements and improved reconstructability.

To compute this metric, we sample spectra \mathbf{y} from a uniform distribution over pixels in a publicly available hyperspectral dataset [18]. We use precise SSFs for our smartphone cameras and spectrophotometer-measured filter transmittances (see Sec. A.1 for details). The final filter pair (Fig. 9 in Supp.) is selected as the one that minimizes $v(\mathbf{F})$.

To verify effectiveness of the proposed filter selection strategy, we trained the MI-HSR method in simulated settings with 12 different filter sets. See Sec. A.2 for details.

4 Doomer Dataset

Overview To support training and evaluation for the MI-HSR task introduced in Sec. 3, we collect a new dataset, which we call *Doomer*¹. Existing hyperspectral datasets are not suited for our setup: none provide spatially misaligned multi-view real RGB observations. Furthermore, no existing dataset aligns with our specific hardware configuration (a triple-camera smartphone with custom spectral filters), making new data collection a necessity.

Doomer contains 155 real-world scenes captured using a Huawei Mate 40 Pro smartphone equipped with Main, Tele, and Wide cameras, along with a Specim IQ hyperspectral camera for ground truth. In each scene, we record three smartphone RAW images, two with custom spectral filters and one unfiltered as well as a 111-band (400 – 730 nm) hyperspectral image. Example captures are shown in Fig. 2.

To provide representability, scenes include a mix of indoor and outdoor environments under varying illumination conditions (e.g., halogen and LED lighting indoors; overcast and sunny weather outdoors), and span a range of objects including food, printed material, architectural surfaces, and color calibration charts. Each scene includes a gray ball reference for future work on illumination estimation. While the gray ball is visible in Wide and Main cameras, it falls outside the Tele field of view

¹The name *Doomer* is inspired by the subcultural aesthetic: most scenes were collected under gloomy or overcast weather conditions, in contrast to the brightly lit existing datasets.

and is cropped out during preprocessing. Non-preprocessed RAW data versions will be included in the public release.

Gray ball reference makes the proposed dataset potentially useful in research on illumination estimation, automatic white balance and color space transform (see Sec. A.3 for more detailed proposals).

Capture setup The data acquisition rig consists of a Specim IQ hyperspectral camera, a Huawei Mate 40 Pro smartphone mounted in a 3D-printed case with slots for spectral filters and a gray reference sphere (VFX ball).

The entire system is mounted on a tripod, with the phone positioned to rotate along a vertical axis for alternating captures (Fig. 3). This design allows the smartphone and hyperspectral camera to image scenes from nearly identical viewpoints, minimizing parallax and occlusion. The gray ball is connected to a rigid rod that allows to regulate the position of the ball in the scene.

Image acquisition proceeds sequentially: first, all three smartphone cameras capture RAW images; then, the smartphone case is moved to make hyperspectral image. Most smartphone settings (e.g., ISO, shutter speed) are controlled automatically, except in scenes with poor red signal where we manually adjusted Tele exposure to avoid excessive noise.

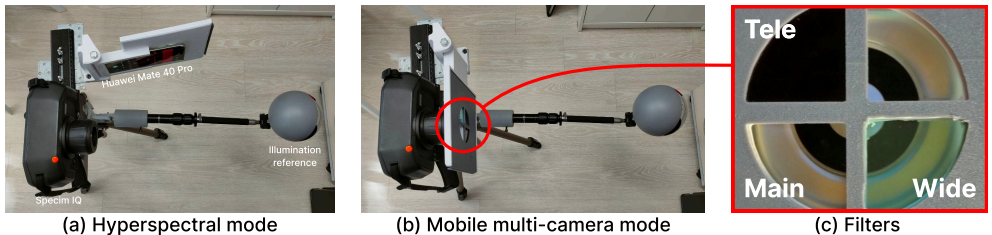


Figure 3: *Capture setup for the Doomer dataset.* (a) Smartphone holder rotated to allow hyperspectral capture via Specim IQ. (b) Smartphone repositioned for simultaneous multi-camera RGB capture. (c) External spectral filters mounted on Tele and Wide cameras to induce spectral diversity.

Data preprocessing Each four-image scene group (three RGB + one HSI) undergoes standardized preprocessing (see Sec. A.3). We also normalize field of view and resolution across sensors. Specifically, we estimate pairwise homographies between each RGB image and the Tele view using SIFT keypoints and RANSAC. All images are then warped to the Tele frame and cropped accordingly. When automatic registration fails, manual alignment is used. Despite this correction, residual geometric misalignment remains due to parallax and non-planar scene structure — motivating our use of alignment-aware HSR models. Finally, all images are downsampled to match the hyperspectral resolution, originally 194×259 cropped to 192×256 for convenience, and spectral grid is resampled to conventional 400–730 nm, $n = 34$, to optimize computational costs.

5 Method

The task of MI-HSR involves predicting a hyperspectral image $\mathbf{Y} \in \mathbb{R}^{h \times w \times n}$ aligned to a reference RGB image $\mathbf{X}_0 \in \mathbb{R}^{h \times w \times 3}$ given also auxiliary RGB images $\{\mathbf{X}_i\}_{i=1}^{k-1} \subset \mathbb{R}^{h \times w \times 3}$ from multiple spatially offset sensors. This setup introduces two key challenges: (i) the available hyperspectral supervision \mathbf{Y} is not aligned with any RGB input, and (ii) the input views are misaligned due to differing camera geometries. Our approach (Fig. 4) addresses both issues, one through pre-processing, the other through architectural design.

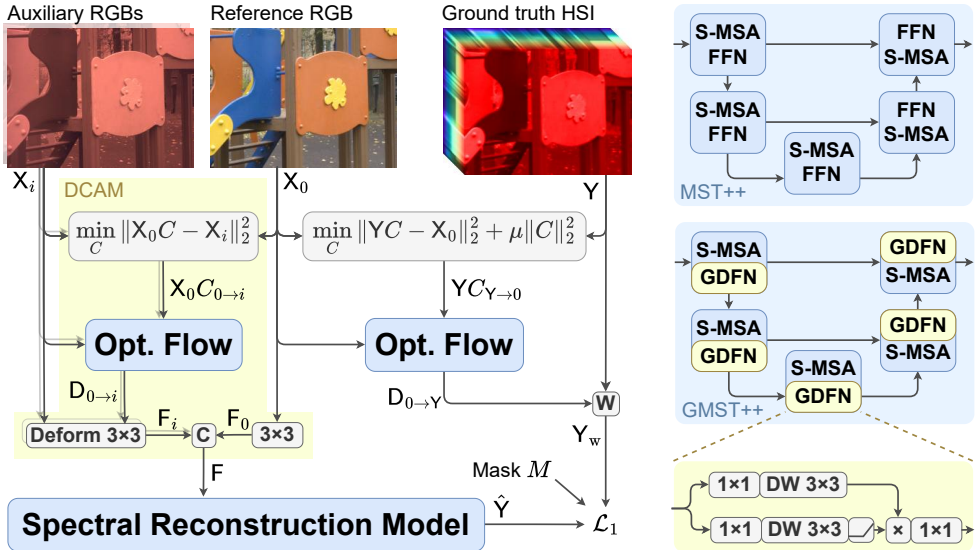


Figure 4: (Left) Our proposed framework with the Deformable Convolution Alignment Module (DCAM) for solving MI-HSR; any existing HSR network can be plugged. (Right) The proposed GMST++ model featuring GDFN module [39].

5.1 Supervision Warping via Optical Flow

To leverage target hyperspectral image for training, we align it to the reference RGB view using pre-trained optical flow (OF). Since spectral and RGB images differ in modality, we first compute a color projection:

$$C_{Y \rightarrow 0} := \arg \min_{C \in \mathbb{R}^{n \times 3}} \|Y C - X_0\|_2^2 + \mu \|C\|_2^2.$$

$Y C_{Y \rightarrow 0}$ serves as an approximation of \mathbf{Y} in the color space of the reference RGB. We noted that the approximation becomes noisy in the absence of the regularization term due to ill-posedness of the problem. Since now both views share the same color space, we can estimate a dense correspondence field $\mathbf{D}_{0 \rightarrow Y} \in \mathbb{R}^{h \times w \times 2}$ using a pre-trained OF

model [40]:

$$\mathbf{D}_{0 \rightarrow Y} := \text{OF}(\mathbf{X}_0, \mathbf{Y}C_{Y \rightarrow 0}).$$

This flow is used to warp the hyperspectral ground truth (GT) to the reference view:

$$\mathbf{Y}_w := \text{Warp}(\mathbf{Y}, \mathbf{D}_{0 \rightarrow Y}), \quad \mathbf{M} := \lfloor \text{Warp}(\mathbf{E}, \mathbf{D}_{0 \rightarrow Y}) \rfloor,$$

where \mathbf{M} is a binary mask indicating valid visible pixels, \mathbf{E} is matrix of ones. This enables aligned supervision for training and point-wise loss computation $\mathcal{L}_1(\hat{\mathbf{Y}} \odot \mathbf{M}, \mathbf{Y}_w \odot \mathbf{M})$

5.2 Deformable Convolution Alignment

Even with warped supervision, the three input views remain spatially misaligned. Direct flow-based registration is possible but leads to unnecessary error accumulation. Instead, one would prefer leveraging the misaligned views “as-is” in some flow-aware manner. To this end, we make use of deformable convolutions [41], which we feed with dense correspondence field between inputs computed by OF. This allows the convolution layer to deterministically shift each of its 3×3 sampling positions toward geometrically matched locations at an auxiliary view and produce a feature map aligned to the reference view. The kernel weights remain learnable, which allows the filter to handle residual local misalignments and simultaneously learn features useful for further spectral reconstruction.

Similar to the previous section, we first unify color spaces of the reference and auxiliary inputs and compute optical flow between them:

$$\begin{aligned} \mathbf{C}_{0 \rightarrow i} &:= \arg \min_{\mathbf{C} \in \mathbb{R}^{3 \times 3}} \|\mathbf{X}_0 \mathbf{C} - \mathbf{X}_i\|_2^2, & i = 1, \dots, k-1, \\ \mathbf{D}_{0 \rightarrow i} &:= \text{OF}(\mathbf{X}_0 \mathbf{C}_{0 \rightarrow i}, \mathbf{X}_i), & i = 1, \dots, k-1. \end{aligned}$$

This time we do not need regularization because channels in \mathbf{X}_0 are not as highly correlated as in \mathbf{Y} . The reference input \mathbf{X}_0 is then passed through a standard 3×3 convolution layer, while the auxiliary inputs \mathbf{X}_i are passed through the aforementioned deformable convolution together with their corresponding deformation fields:

$$\mathbf{F}_0 := \text{Conv}(\mathbf{X}_0), \quad \mathbf{F}_i := \text{DeformConv}(\mathbf{X}_i, \mathbf{D}_{0 \rightarrow i}).$$

Because DeformConv employs a 3×3 kernel, it needs 3×3 sampling points per output pixel. The deformation field supplies only the central offset; the other eight offsets are fixed relative shifts $(-1, -1)$, $(-1, 0)$, ..., $(+1, +1)$ applied around it. Concatenation of all feature maps $\{\mathbf{F}_i\}_{i=0}^{k-1}$ serves as an input for Spectral Reconstruction module.

5.3 Spectral Reconstruction

We employ a UNet-like architecture Gated Multi-Stage Transformer (GMST++) heavily inspired by MST++ [8]. Its main building block is Spectral Transformer

(ST) block, which in turn consists of Spectral Multi-head Self-attention (S-MSA) and the Gated DConv Feed-forward Network (GDFN) adopted from Restormer [39]. S-MSA treats each 2D slice of the feature tensor as a token and computes attention across channels based on their global correlations. GDFN comprises two branches of successive 1×1 and depth-wise 3×3 convolutions; one branch is GeLU-activated and then multiplied by the other, thereby attenuating some spatial locations and amplifying others. This is particularly helpful in multi-image setting, where small residual misalignments may remain, and their attenuation prevents them from misleading the reconstruction process.

6 Experiments

Our main intention is to demonstrate the superiority of leveraging a multi-camera imaging system for HSR over reconstruction from a single RGB alone. We evaluate this in both Clean and Real-world settings. The Clean setting consists of simulating perfectly aligned RGB images from a widely recognised HSI benchmark. Such a controlled setup allows us to isolate the effect of increasing the number of cameras and serves as a proof of concept for our proposed acquisition system. The Real-world setting verifies our misalignment-aware framework and shows that the advantages of a multi-camera system can be retained even in an uncontrolled environment.

6.1 Experimental Setup

Datasets The Clean setting employs Arad 1K dataset [19] as the source of ground truth HSIs. We simulate three input RGBs given camera response functions of Samsung Galaxy S20, Google Pixel, and iPhone 11 [42]. The spectral filters set was selected specifically for this camera configuration following the methodology described in Sec. 3.2, including leaving the first camera without the filter. Sensor noise was injected according to Gaussian-Poisson model [43]. The Real-world setting employs our *Doomer* dataset as it is currently the only available dataset suitable for MI-HSR. We split *Doomer* into *train* and *test* in proportion 4:1 and use the authors-provided split for Arad 1K.

Methods We choose several state-of-the-art HSR methods for comparison with GMST++: AWAN [44], MST++ [8], and SPECAT [27]. Among general image restoration models, we additionally include NAFNet [45]. To evaluate these models in Real-world Multi-image setting, we prepend them with our DCAM module.

Metrics We adopt the well-known Peak Signal-to-Noise Ratio (PSNR) and Spectral Angle Mapper (SAM). We additionally introduce the Normalized Spectral Error (NSE), which serves as an alternative to MRAE since it does not penalize small values of individual bands and better reflects the integral nature of radiance:

$$\text{NSE}(\hat{\mathbf{y}}, \mathbf{y}) = \frac{\|\hat{\mathbf{y}} - \mathbf{y}\|_1}{\|\mathbf{y}\|_1} \cdot 100\%, \quad \hat{\mathbf{y}}, \mathbf{y} \in \mathbb{R}^n.$$

In the warped GT, some pixels become missing or invalid, as indicated by the mask \mathbf{M} . Locations where $\mathbf{M}_{i,j} = 0$ are excluded from the metric computations.

Implementation details In all the experiments we used Adam optimizer with learning rate of 0.0004. During training, each image was randomly cropped to 64×64 and optionally flipped vertically or horizontally. Number of epochs was set to 2000 for the Clean setting and to 10000 for the Real-world. Every 30 epochs we ran evaluation loop; the final model is the one with the best MAE on the test set.

6.2 Results

We trained and tested all HSR methods using two input configurations: single-image $\{\mathbf{X}_0\}$ and multi-image $\{\mathbf{X}_0, \mathbf{X}_1, \mathbf{X}_2\}$. The quantitative result for the Clean and Real-world settings are listed in Tables 2 and 3, respectively. Note that we report the number of *trainable* parameters which means the pre-trained weights of PWC-Net are not counted. However, we do count PWC-Net’s contribution in GMACs.

Method	PSNR, dB \uparrow	SAM, $^\circ$ \downarrow	NSE, % \downarrow	Params, K	GMACs
<i>Single-image input</i>					
AWAN [44]	33.91	4.19	7.31	525	25.82
MST++ [8]	<u>33.98</u>	4.06	7.12	546	31.20
SPECAT [27]	33.63	4.17	7.34	346	53.32
NAFNet [45]	33.84	<u>4.14</u>	7.36	372	1.50
GMST++ (ours)	33.99	4.15	<u>7.25</u>	546	31.29
<i>Multi-image input</i>					
AWAN [44]	<u>41.98</u>	2.69	4.76	527	44.05
MST++ [8]	41.78	2.56	<u>4.63</u>	547	31.62
SPECAT [27]	39.44	3.05	5.54	350	54.22
NAFNet [45]	41.27	<u>2.63</u>	4.83	373	19.68
GMST++ (ours)	42.17	2.47	4.51	547	31.71

Table 2: Results in Clean setting (Arad 1K dataset). **Best** and second-best results are highlighted.

Table 2 shows superiority of our GMST++ in multi-image configuration, though it outperforms its nearest competitor only by 0.2 dB. Overall, multi-image input allows substantially better reconstruction than from single-image suggesting that our filtering device design unveils lots of spectral information previously hidden in single RGB inputs.

In Real-world setting of Table 3 the MI-HSR by our DCAM + GMST++ method reaches 31.46 PSNR, which is +0.7 dB higher than its nearest competitor and at least +2.44 dB better than any method operating on single-image inputs. The latter improvement secures applicability of multi-image approach in practice. Notably, within the single-image setting our method is far from the best performer, which highlights its

Method	PSNR, dB \uparrow	SAM, $^\circ$ \downarrow	NSE, % \downarrow	Params, K	GMACs
<i>Single-image input</i>					
AWAN [44]	28.65	5.97	12.58	525	25.82
MST++ [8]	<u>28.91</u>	5.23	11.57	655	7.35
SPECAT [27]	27.91	6.09	12.12	389	11.21
NAFNet [45]	29.02	5.39	<u>11.72</u>	372	1.50
GMST++	28.86	<u>5.28</u>	12.14	654	7.37
<i>Multi-image input</i>					
DCAM + AWAN [44]	29.66	4.37	10.45	527	44.06
DCAM + MST++ [8]	<u>30.71</u>	<u>4.19</u>	<u>9.44</u>	657	25.59
DCAM + SPECAT [27]	30.34	4.50	9.72	393	29.54
DCAM + NAFNet [45]	30.53	4.33	9.85	373	19.69
DCAM + GMST++	31.46	3.91	8.35	658	25.61

Table 3: Results in Real-world setting (Doomer dataset). All methods are supervised by warped GT (\mathbf{Y}_w). To let the methods handle multiple misaligned inputs, we prepend them with our DCAM module. **Best** and second-best results are highlighted.

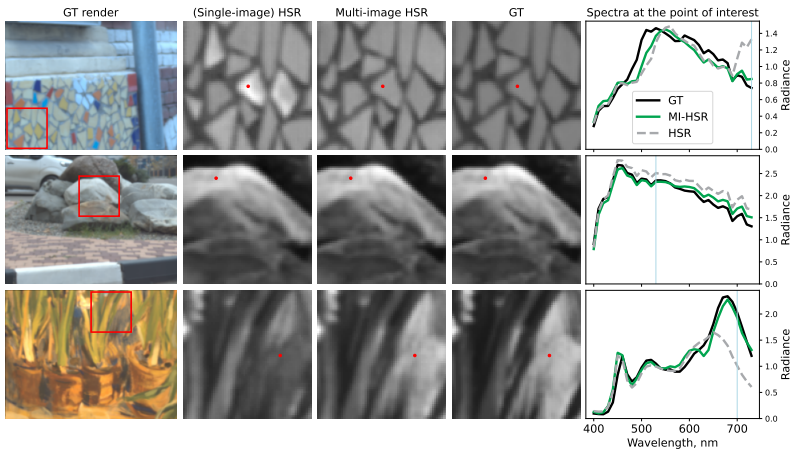


Figure 5: Qualitative comparison of GMST++ and DCAM + GMST++ predictions under single-image and multi-image input settings respectively. For each scene, a specific spectral band, region of interest, and point of interest are selected. Grayscale renderings correspond to a specific spectral band (indicated in blue on spectral plot). Colorful GT renderings are done with CIE RGB CMFs.

tailoring specifically for MI-HSR. Indeed, our motivation for incorporating the GDFN block was to attenuate misaligned regions. In the absence of such misalignments, the model may suppress locally useful information.

We show qualitative performance of our framework based on patch-level comparisons at a selected wavelength as well as radiance profiles at specific points of interest in Fig. 5. The multi-camera system consistently recovers more plausible

surface details than the single-camera setup. In the first and third rows, single-camera pipeline misestimates a specific region at a specific wavelength band (730 and 700 nm respectively). In the second row, single-camera pipeline lags behind in overall estimation of brightness, though correctly recovering the shape of the spectrum. These results highlight the improved both spatial and spectral fidelity enabled by multi-view fusion in the MI-HSR system.

6.3 Ablation Study

To assess importance of each component in our framework, we perform an ablation study by either replacing GDFN with Feed-Forward Network (fallback to MST++) or removing the DCAM module along with the optical flow network in it. All evaluations are performed under Real-world Multi-input setting and are shown in Table 4.

DCAM	GDFN	PSNR, dB \uparrow	SAM, $^\circ$ \downarrow	NSE, % \downarrow
		28.91	5.23	11.57
	+	30.76	4.41	9.62
+		30.71	4.19	9.44
+	+	31.46	3.91	8.35

Table 4: Impact of various architecture components on the overall reconstruction quality. Evaluated on the Doomer dataset. **Best** results are highlighted.

6.4 What is the best possible quality?

Even professional hyperspectral equipment has its own precision, which limits best achievable quality as a GT. Hyperspectral image registration is a process of registering photons, which means our GTs are inherently noisy just like consumer CMOS sensors. To quantify this boundary, we captured series of HSIs of static scenes with color charts under two different light conditions. The metrics were calculated between a fixed image from a series and the average of remain images, see Tab. 5. The estimated values should be interpreted as approximate bound for any MI-MSR network trained and tested on Doomer dataset. Comparable metric values may indicate overfitting or sensitivity to sensor noise.

Light conditions	PSNR, dB \uparrow	SAM, $^\circ$ \downarrow	NSE, % \downarrow
Bright scenario (outdoor sunny)	41.60 \pm 3.41	0.71 \pm 0.11	3.00 \pm 0.71
Medium brightness (indoor LED)	37.82 \pm 3.51	1.02 \pm 0.13	4.45 \pm 1.28

Table 5: Mean and variance of Specim IQ shots of the same scene.

7 Conclusion

This work rethinks HSR through the lens of practical acquisition. By moving beyond single RGB image constraints, we demonstrate that leveraging multiple smartphone cameras with carefully chosen spectral filters can significantly enrich the input signal and reduce ambiguity in reconstruction.

The introduction of the Doomer dataset marks an important step forward for benchmarking in this space, enabling systematic evaluation of multi-view HSR under realistic conditions. Empirical results validate both our hardware configuration and model design, suggesting a promising direction for low-cost, deployable hyperspectral imaging systems. Proposed Deformable Convolution Alignment Module and conducted experiments show the alignment importance in the MI-HSR task, while proposed GMST++ is comparable with other state-of-the-art methods in established single image HSR it shows spectral reconstruction improvement in multi-image input even without DCAM.

Looking ahead, we aim to further explore the temporal dimension for dynamic scenes, optimize for energy-efficient mobile deployment, and investigate more principled learning paradigms under limited supervision or device mismatch.

References

- [1] Xiang Xu, Jun Li, Xin Huang, Mauro Dalla Mura, and Antonio Plaza. Multiple morphological component analysis based decomposition for remote sensing image classification. *IEEE Transactions on Geoscience and Remote Sensing*, 54(5):3083–3102, 2016.
- [2] Meiling Wang, Yongchang Xu, Zhisheng Wang, and Changda Xing. Deep margin cosine autoencoder-based medical hyperspectral image classification for tumor diagnosis. *IEEE Transactions on Instrumentation and Measurement*, 72:1–12, 2023.
- [3] Seon Joo Kim, Fanbo Deng, and Michael S Brown. Visual enhancement of old documents with hyperspectral imaging. *Pattern Recognition*, 44(7):1461–1469, 2011.
- [4] Kailai Zhou, Lijing Cai, Yibo Wang, Mengya Zhang, Bihan Wen, Qiu Shen, and Xun Cao. Joint rgb-spectral decomposition model guided image enhancement in mobile photography. In *Proceedings of the IEEE/CVF European Conference on Computer Vision*. Springer, 2024.
- [5] Ortal Glatt, Yotam Ater, Woo-Shik Kim, Shira Werman, Oded Berby, Yael Zini, Shay Zelinger, Sangyoon Lee, Heejin Choi, and Evgeny Soloveichik. Beyond rgb: a real world dataset for multispectral imaging in mobile devices. In *Proceedings of the IEEE/CVF Winter Conference on Applications of Computer Vision*, 2024.
- [6] Da-Wen Sun, Hongbin Pu, and Jingxiao Yu. Applications of hyperspectral imaging technology in the food industry. *Nature Reviews Electrical Engineering*, 1(4):251–263, 2024.
- [7] Md Toukir Ahmed, Ocean Monjur, and Mohammed Kamruzzaman. Deep learning-based hyperspectral image reconstruction for quality assessment of agro-product. *Journal of Food Engineering*, 382:112223, 2024.

- [8] Yuanhao Cai, Jing Lin, Zudi Lin, Haoqian Wang, Yulun Zhang, Hanspeter Pfister, Radu Timofte, and Luc Van Gool. Mst++: Multi-stage spectral-wise transformer for efficient spectral reconstruction. In *Proceedings of the IEEE/CVF Conference on Computer Vision and Pattern Recognition*, 2022.
- [9] Yuzhi Zhao, Lai-Man Po, Qiong Yan, Wei Liu, and Tingyu Lin. Hierarchical regression network for spectral reconstruction from rgb images. In *Proceedings of the IEEE/CVF Conference on Computer Vision and Pattern Recognition Workshops*, 2020.
- [10] Renjie Wu, Yuqi Li, Xijiong Xie, and Zhijie Lin. Optimized multi-spectral filter arrays for spectral reconstruction. *Sensors*, 19(13):2905, 2019.
- [11] Shijie Nie, Lin Gu, Yinqiang Zheng, Antony Lam, Nobutaka Ono, and Imari Sato. Deeply learned filter response functions for hyperspectral reconstruction. In *Proceedings of the IEEE/CVF Conference on Computer Vision and Pattern Recognition*, 2018.
- [12] Ying Fu, Tao Zhang, Yinqiang Zheng, Debing Zhang, and Hua Huang. Joint camera spectral sensitivity selection and hyperspectral image recovery. In *Proceedings of the IEEE/CVF the European Conference on Computer Vision*, 2018.
- [13] Neha Sharma, Muhammad Shahzaib Waseem, Shahrzad Mirzaei, and Mohamed Hefeeda. Mobispectral: Hyperspectral imaging on mobile devices. In *Proceedings of the 29th Annual International Conference on Mobile Computing and Networking*, 2023.
- [14] Seoung Wug Oh, Michael S Brown, Marc Pollefeys, and Seon Joo Kim. Do it yourself hyperspectral imaging with everyday digital cameras. In *Proceedings of the IEEE/CVF Conference on Computer Vision and Pattern Recognition*, 2016.
- [15] Fumihito Yasuma, Tomoo Mitsunaga, Daisuke Iso, and Shree K Nayar. Generalized assorted pixel camera: postcapture control of resolution, dynamic range, and spectrum. *IEEE transactions on image processing*, 19(9):2241–2253, 2010.
- [16] Ayan Chakrabarti and Todd Zickler. Statistics of real-world hyperspectral images. In *Proceedings of the IEEE/CVF Winter Conference on Applications of Computer Vision*, 2011.
- [17] Boaz Arad and Ohad Ben-Shahar. Sparse recovery of hyperspectral signal from natural rgb images. In *Proceedings of the IEEE/CVF the European Conference on Computer Vision*, 2016.
- [18] Yuqi Li, Qiang Fu, and Wolfgang Heidrich. Multispectral illumination estimation using deep unrolling network. In *Proceedings of the IEEE/CVF International Conference on Computer Vision*, 2021.
- [19] Boaz Arad and Radu Timofte. Ntire 2022 spectral recovery challenge and data set. In *Proceedings of the IEEE/CVF Conference on Computer Vision and Pattern Recognition*, 2022.
- [20] Stephan Helling, Enrico Seidel, and Wolfram Biehlig. Algorithms for spectral color stimulus reconstruction with a seven-channel multispectral camera. In *Conference on Colour in Graphics, Imaging, and Vision*. Society of Imaging Science and Technology, 2004.

- [21] Eva M Valero, Juan L Nieves, Sergio MC Nascimento, Kinjiro Amano, and David H Foster. Recovering spectral data from natural scenes with an rgb digital camera and colored filters. *Color Research & Application*, 32(5):352–360, 2007.
- [22] Jonas Aeschbacher, Jiqing Wu, and Radu Timofte. In defense of shallow learned spectral reconstruction from rgb images. In *Proceedings of the IEEE/CVF International Conference on Computer Vision Workshops*, 2017.
- [23] Yan Jia, Yinqiang Zheng, Lin Gu, Art Subpa-Asa, Antony Lam, Yoichi Sato, and Imari Sato. From rgb to spectrum for natural scenes via manifold-based mapping. In *Proceedings of the IEEE/CVF International Conference on Computer Vision*, 2017.
- [24] David H Foster, Kinjiro Amano, Sérgio MC Nascimento, and Michael J Foster. Frequency of metamerism in natural scenes. *Journal of the Optical Society of America A*, 23(10):2359–2372, 2006.
- [25] Silvano Galliani, Charis Lanaras, Dimitrios Marmanis, Emmanuel Baltsavias, and Konrad Schindler. Learned spectral super-resolution. *arXiv preprint arXiv:1703.09470*, 2017.
- [26] Zhan Shi, Chang Chen, Zhiwei Xiong, Dong Liu, and Feng Wu. Hscnn+: Advanced cnn-based hyperspectral recovery from rgb images. In *Proceedings of the IEEE/CVF Conference on Computer Vision and Pattern Recognition Workshops*, 2018.
- [27] Zhiyang Yao, Shuyang Liu, Xiaoyun Yuan, and Lu Fang. Specat: Spatial-spectral cumulative-attention transformer for high-resolution hyperspectral image reconstruction. In *Proceedings of the IEEE/CVF Conference on Computer Vision and Pattern Recognition*, pages 25368–25377, 2024.
- [28] Xingxing Yang, Jie Chen, and Zaifeng Yang. Unraveling metameric dilemma for spectral reconstruction: A high-fidelity approach via semi-supervised learning. In *The Thirty-ninth Annual Conference on Neural Information Processing Systems*, 2025.
- [29] Miaoyu Li, Ying Fu, Tao Zhang, Ji Liu, Dejing Dou, Chenggang Yan, and Yulun Zhang. Latent diffusion enhanced rectangle transformer for hyperspectral image restoration. *IEEE Transactions on Pattern Analysis and Machine Intelligence*, 2024.
- [30] Qiang Fu, Matheus Souza, Eunsue Choi, Suhyun Shin, Seung-Hwan Baek, and Wolfgang Heidrich. Limitations of data-driven spectral reconstruction: An optics-aware analysis. *IEEE Transactions on Computational Imaging*, 2025.
- [31] Tae Hyun Kim, Mehdi SM Sajjadi, Michael Hirsch, and Bernhard Scholkopf. Spatio-temporal transformer network for video restoration. In *Proceedings of the IEEE/CVF European Conference on Computer Vision*, 2018.
- [32] Kelvin CK Chan, Xintao Wang, Ke Yu, Chao Dong, and Chen Change Loy. Basicvsr: The search for essential components in video super-resolution and beyond. In *Proceedings of the IEEE/CVF Conference on Computer Vision and Pattern Recognition*, 2021.
- [33] Yapeng Tian, Yulun Zhang, Yun Fu, and Chenliang Xu. Tdan: Temporally-deformable alignment network for video super-resolution. In *Proceedings of the IEEE/CVF Conference on Computer Vision and Pattern Recognition*, 2020.

- [34] Xintao Wang, Kelvin CK Chan, Ke Yu, Chao Dong, and Chen Change Loy. Edvr: Video restoration with enhanced deformable convolutional networks. In *Proceedings of the IEEE/CVF Conference on Computer Vision and Pattern Recognition Workshops*, pages 0–0, 2019.
- [35] Tengfei Wang, Jiaxin Xie, Wenxiu Sun, Qiong Yan, and Qifeng Chen. Dual-camera super-resolution with aligned attention modules. In *Proceedings of the IEEE/CVF International Conference on Computer Vision*, 2021.
- [36] Zhilu Zhang, Haolin Wang, Ming Liu, Ruohao Wang, Jiawei Zhang, and Wangmeng Zuo. Learning raw-to-srgb mappings with inaccurately aligned supervision. In *Proceedings of the IEEE/CVF International Conference on Computer Vision*, 2021.
- [37] Omar Elezabi, Zongwei Wu, and Radu Timofte. Enhanced super-resolution training via mimicked alignment for real-world scenes. In *Proceedings of the Asian Conference on Computer Vision*, 2024.
- [38] Daniil Reutskii and Egor Ershov. Spectral filters design for a better hyperspectral reconstruction. In *Sixteenth International Conference on Machine Vision (ICMV 2023)*. SPIE, 2024.
- [39] Syed Waqas Zamir, Aditya Arora, Salman Khan, Munawar Hayat, Fahad Shahbaz Khan, and Ming-Hsuan Yang. Restormer: Efficient transformer for high-resolution image restoration. In *Proceedings of the IEEE/CVF conference on computer vision and pattern recognition*, pages 5728–5739, 2022.
- [40] Deqing Sun, Xiaodong Yang, Ming-Yu Liu, and Jan Kautz. Pwc-net: Cnns for optical flow using pyramid, warping, and cost volume. In *Proceedings of the IEEE/CVF Conference on Computer Vision and Pattern Recognition*, 2018.
- [41] Jifeng Dai, Haozhi Qi, Yuwen Xiong, Yi Li, Guodong Zhang, Han Hu, and Yichen Wei. Deformable convolutional networks. In *Proceedings of the IEEE/CVF International Conference on Computer Vision*, 2017.
- [42] Shoji Tominaga, Shogo Nishi, and Ryo Ohtera. Measurement and estimation of spectral sensitivity functions for mobile phone cameras. *Sensors*, 21(15):4985, 2021.
- [43] Alessandro Foi, Mejdi Trimeche, Vladimir Katkovnik, and Karen Egiazarian. Practical poissonian-gaussian noise modeling and fitting for single-image raw-data. *IEEE transactions on image processing*, 17(10):1737–1754, 2008.
- [44] Jiaojiao Li, Chaoxiong Wu, Rui Song, Yunsong Li, and Fei Liu. Adaptive weighted attention network with camera spectral sensitivity prior for spectral reconstruction from rgb images. In *Proceedings of the IEEE/CVF Conference on Computer Vision and Pattern Recognition Workshops*, 2020.
- [45] Liangyu Chen, Xiaojie Chu, Xiangyu Zhang, and Jian Sun. Simple baselines for image restoration. In *European conference on computer vision*, pages 17–33. Springer, 2022.
- [46] Egor Ershov, Vasily Tesalin, Ivan Ermakov, and Michael S Brown. Physically-plausible illumination distribution estimation. In *Proceedings of the IEEE/CVF International Conference on Computer Vision*, 2023.

- [47] Hongkai Chen, Zixin Luo, Lei Zhou, Yurun Tian, Mingmin Zhen, Tian Fang, David Mckinnon, Yanghai Tsin, and Long Quan. Aspanformer: Detector-free image matching with adaptive span transformer. In *European conference on computer vision*, pages 20–36. Springer, 2022.
- [48] Zachary Teed and Jia Deng. Raft: Recurrent all-pairs field transforms for optical flow. In *European conference on computer vision*, pages 402–419. Springer, 2020.

A Technical Appendices and Supplementary Material

To ensure disambiguation, here is the list of some designations used throughout the main paper and this document:

- Photometric normalization — division of a camera sensor signal by ISO (if applicable) and exposure time. Black current subtraction is also applied beforehand.
- \mathbf{x} — a photometrically normalized signal (probably noisy) from smartphone camera(s). Can be $\in \mathbb{R}^3$ or $\in \mathbb{R}^{3k}$ depending on context.
- $\bar{\mathbf{x}}$ — a photometrically normalized signal as it would be in an ideal world without noise.
- \mathbf{y} — a photometrically normalized radiance spectrum. Is assumed to be noiseless (however, in Sec. 6.4 of the main paper we discuss the outcomes of this assumption).

A.1 Estimation of Spectral Sensitivity Functions and Transmittance Functions

Spectral sensitivity functions. To estimate SSF of a smartphone camera, we acquired 25 sample pairs of $\mathbf{x}_i \in \mathbb{R}^3$ and $\mathbf{y}_i \in \mathbb{R}^n$ corresponding to flat-field illumination (FFI) of narrow-band LED light sources in an integrating sphere. For each LED i , we took a photo of FFI (Fig. 6), extracted the central 100×100 patch from it, photometrically normalized it and computed the channel-wise average to get \mathbf{x}_i . Then we measured the LED radiance spectrum \mathbf{y}_i using an X-Rite i1 Pro spectrophotometer with the help of `spotread` routine from Argyll color management system.

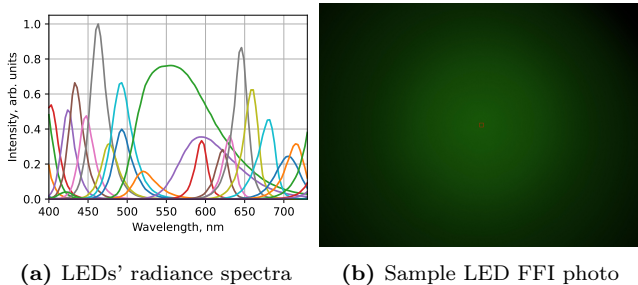


Figure 6: Training data for SSF estimation: (a) spectra of 25 LEDs measured using X-Rite i1 Pro; (b) an example of raw FFI photo. Notice the vignetting effect. To mitigate this effect, channel-wise average of a tiny central patch (in red) was used as a sample \mathbf{x}_i

Given the measurements $\{\mathbf{x}_i, \mathbf{y}_i\}_{i=1}^{25}$, the spectral sensitivities estimation problem

can be formulated as a regularized quadratic optimization problem:

$$\begin{aligned} \min_{\mathbf{C}} \quad & \sum_{i=1}^{25} \|\mathbf{x}_i - \mathbf{C}^\top \mathbf{y}_i\|_2^2 + \lambda \|\mathbf{D}\mathbf{C}\|_2^2 \\ \text{s. t.} \quad & \mathbf{C} \geq 0 \end{aligned} \tag{1}$$

where the regularization term $\lambda \|\mathbf{D}\mathbf{C}\|_2^2$ imposes smoothness, \mathbf{D} is the second-order derivative operator. The objective (1) was minimized using the Adam optimizer.

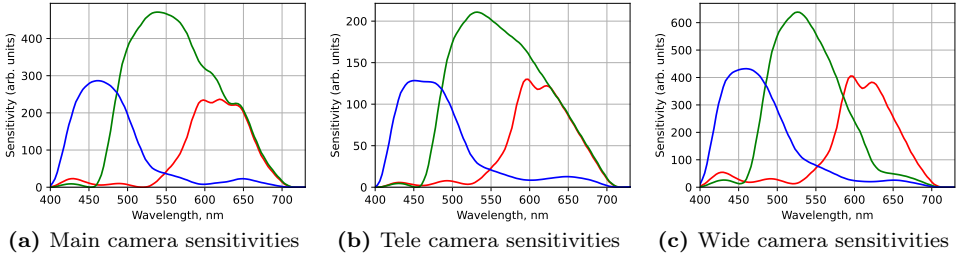


Figure 7: Estimated smartphone cameras spectral sensitivities.

To validate the estimated $\hat{\mathbf{C}}$, we captured a color rendition chart by the Specim IQ hyperspectral camera and all three smartphone cameras. The HSI was calibrated (more on that in the next paragraph) and projected onto each camera’s sensor space to yield RGB predictions. We compared the predicted and actual RGBs of the color patches: pixels of a patch were pixel-wise averaged (Fig. 12 gives a sight on how such patches look like). The average angular error of color reproduction was $\approx 1^\circ$ — indistinguishable to a human eye.

Specim IQ calibration. Spectral measurements of X-Rite i1 Pro and Specim IQ are actually inconsistent. It is not surprising: Specim IQ is not designed to be photometrically accurate. Instead, it allows to estimate band-wise relations between the *calibration target* in a scene and other objects. However, if we estimate the band-wise calibration divisor between X-Rite i1 Pro and Specim IQ, we can further use it to obtain physically-correct HSIs. We illuminated the integration sphere using a mixture of LEDs that yields even spectral power distribution, obtained X-Rite and Specim IQ measurements of it and divided one by another:

$$\mathbf{k} = \mathbf{y}_{\text{specim}} \oslash \mathbf{y}_{\text{xrite}},$$

The divisor is applied to every HSI filmed by the Specim IQ in this research.

Since the operational range of Specim IQ is 400–1000 nm and the one of X-Rite is 380–730 nm, all our spectral measurements are defined on their intersection: 400–730 nm.

Transmittance functions of filters were measured using an SF-2000 spectrophotometer.

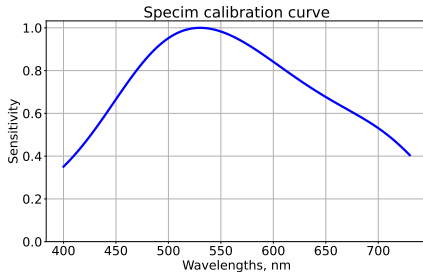


Figure 8: The estimated Specim IQ calibration divisor

A.2 Spectral Uncertainty

The inspiration comes from the well-known conditional entropy $H(\xi | \eta)$, which quantifies the information loss of a latent random variable ξ when observing the outcomes of another random variable η :

$$H(\xi | \eta) = \mathbb{E}_{x \sim \eta} H(\xi | \eta = x), \quad (2)$$

where $H(\xi | \eta = x)$ is the ordinary entropy of ξ given event $\eta = x$. However, entropy is designed especially for discrete-distributed variables of categorical type. When uncertainty of a categorical random variable is indeed best described by the entropy of its distribution, for continuous random variables variance is a better choice. When dealing with random vectors, variance becomes a matrix, so we consider the trace of it as a reasonable summary. If we put the trace of variance instead of the entropy in (2) and substitute $\xi = \mathbf{y}, \eta = \mathbf{x}$, we get the spectral uncertainty of our filters-modified optical system:

$$v(\mathbf{F}) = \mathbb{E}_{\mathbf{x}} [\text{tr } \text{Var}_{\mathbf{y}}(\mathbf{y} | \mathbf{x})],$$

where the dependence on \mathbf{F} is hidden inside the relationship between \mathbf{y} and \mathbf{x} . However, \mathbf{y} and \mathbf{x} are not random variables until we define them so. Let \mathbf{y} have a discrete distribution $p(\mathbf{y}_i)$ over a finite set of radiance spectra $\mathcal{R} = \{\mathbf{y}_1, \dots, \mathbf{y}_N\}$ derived from a dataset of HSIs. Such definition reflects the *a priori* information about natural radiance. In the relation $\mathbf{x} = \mathbf{C}_F \mathbf{r} + \mathbf{n}$ only noise \mathbf{n} is yet to define. Let $\bar{\mathbf{x}} = \mathbf{C}_F \mathbf{y}$ be an unnoised camera response. We model noise as

$$\mathbf{n} | \bar{\mathbf{x}} \sim \mathcal{N}(\mathbf{0}, \Sigma(\bar{\mathbf{x}})), \quad (3)$$

$$\Sigma(\bar{\mathbf{x}}) = \text{diag}[\sigma_1^2(\bar{c}_1); \dots; \sigma_{3k}^2(\bar{c}_{3k})], \quad (4)$$

where $\sigma_i(\cdot)$ is expanded in (5) later in the chapter.

Now, when we defined $p(\mathbf{x} | \mathbf{y})$, we can derive from the Bayesian rule:

$$p(\mathbf{y}_i | \mathbf{x}) = \frac{p(\mathbf{x} | \mathbf{y}_i) p(\mathbf{y}_i)}{\sum_{i=1}^N p(\mathbf{x} | \mathbf{y}_i) p(\mathbf{y}_i)},$$

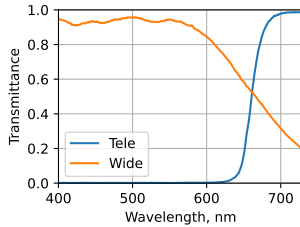


Figure 9: Filters selected for Tele and Wide cameras.

and further:

$$\mathbb{E}_{\mathbf{y}}(\mathbf{y} \mid \mathbf{x}) = \sum_{i=1}^N p(\mathbf{y}_i \mid \mathbf{x}) \mathbf{y}_i,$$

$$\text{tr Var}_{\mathbf{y}}(\mathbf{y} \mid \mathbf{x}) = \sum_{i=1}^N p(\mathbf{y}_i \mid \mathbf{x}) \|\mathbf{y}_i - \mathbb{E}_{\mathbf{y}}(\mathbf{y} \mid \mathbf{x})\|_2^2.$$

Now we have an expression depending on \mathbf{x} which we should take $\mathbb{E}_{\mathbf{x}}$ of. However, this is intractable. So we should resort to Monte Carlo method by sampling \mathbf{x} according to its definition: first take random $\mathbf{y}^* \in \mathcal{R}$, then sample \mathbf{x} from $\mathcal{N}(\mathbf{C}_{\mathbf{F}}\mathbf{y}^*, \Sigma(\mathbf{C}_{\mathbf{F}}\mathbf{y}^*))$. In our experiments, 2^{20} samples were sufficient to achieve 0.5% of relative standard deviation.

To derive \mathcal{R} , we first extracted every 29×29 th pixel of the KAUST dataset [18], which resulted in 559,921 samples. To reduce computational requirements, we compressed \mathcal{R} to the size of $N = 1024$ by running K-Means algorithm and employing clusters' centers. We assigned $p(\mathbf{y}_i)$ to be the share of initial 559,921 radiance spectra that belong to the cluster around \mathbf{y}_i .

The KAUST dataset contains objects reflectance. We correct work with radiance data we sample the illuminant spectra from gray ball after collecting the *Doomer* dataset. In Fig. 10 we show the best filters selected by the criterion after applying typical *Doomer* illumination.

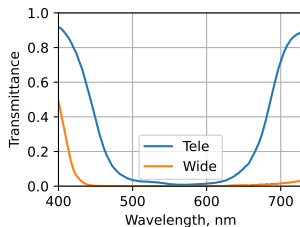


Figure 10: Best filters for typical *Doomer* radiance.

Experimental justification. Having the estimated spectral characteristics of our filtered smartphone cameras setup ($\mathbf{C}_{\mathbf{F}}$) and the sensor noise model (5), we find

ourselves in a position where we can simulate images of the triple-camera setup from HSIs and run experiments on simulated data. Therefore, we can support the proposed spectral uncertainty criterion by simulating input images \mathbf{X}_0 , \mathbf{X}_1 , \mathbf{X}_2 given filters, measuring HSR performance and plotting it against $v(\mathbf{C}_F)$.

We chose 12 random filter pairs and simulated 12 versions of our dataset. For each version, MI-MSFN was trained and evaluated. Fig. 11 shows the dependence of three performance metrics on the proposed spectral uncertainty criterion. A strong correlation is observed, as the Pearson correlation coefficient has an absolute value greater than 0.8.

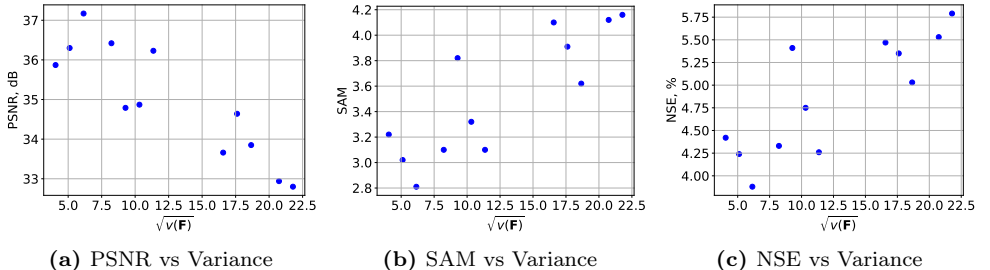


Figure 11: Relation between PSNR, SAM, NSE in simulated settings and the proposed spectral uncertainty criterion.

Noise model. Let \bar{x}_i be a photometrically-normalized ground-truth signal level at channel i , t be exposure time, g be ISO. The expected collected charge at image sensor is $\bar{x}_i t$. Following Foi et al. [43], we model noise of the collected charge as $\varepsilon \sim \mathcal{N}(0, \alpha_i \bar{x}_i t + \beta_i)$, where α_i , β_i are parameters of the model. The final value in the raw image is further amplified by g along with the noise: $(\bar{x}_i t + \varepsilon)g$. Foi et al. also introduce additional noise after amplification, but we neglect it for simplicity. The observed photometrically-normalized signal is then given by:

$$x_i = \frac{(\bar{x}_i t + \varepsilon)g}{tg} = \bar{x}_i + \frac{\varepsilon}{t}.$$

To be consistent with (3) and (4), we define $\sigma_i(x)$ as:

$$\sigma_i(\bar{x}_i) = \frac{\sqrt{\alpha_i \bar{x}_i t + \beta_i}}{t} \quad (5)$$

We estimate parameters α_i , β_i of this model by plotting $\sigma_i t$ against $\bar{x}_i t$ in Fig. 12.

The only problem left in (5) is the hidden dependence on t . Given simulated $\bar{\mathbf{x}} = \mathbf{C}_F \mathbf{y}$, we cannot add noise properly unless we know exposure time t . In real-life setting, exposure time is determined by a camera automatically depending on the brightness of a scene. For simplicity, we model this in a piecewise-power fashion. We gathered 1000 raw images from phone’s gallery and plotted t against the average of photometrically normalized signals across all channels, height and width in an image $x = \frac{1}{h \times w \times 3} \sum_{i,j,k} \mathbf{X}_{i,j,k}$ (Fig. 13). The fitted function allows to estimate t given \bar{x}_i .

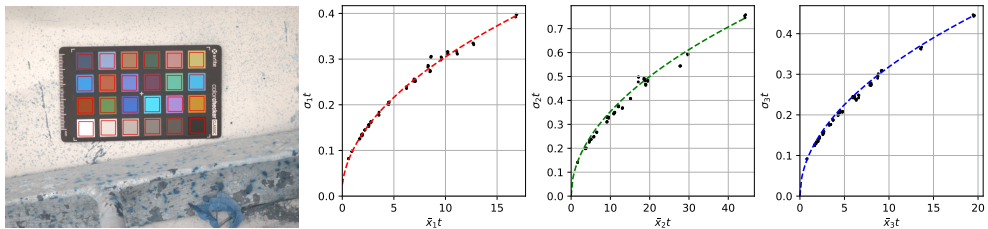


Figure 12: Plotting $\sigma_i t$ against \bar{x}_{it} for the Telephoto camera based on a single shot. Each data point (24 in total) is given by channel-wise mean and std dev of a color patch (left, in red). In each plot, point cloud is approximated by a dashed line (5) using least-squares; each color channel i gets its own noise parameters α_i, β_i (right).

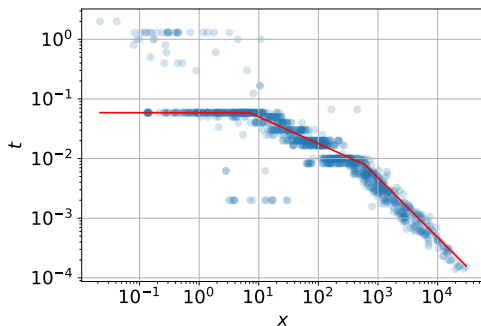


Figure 13: How exposure time depends on scene brightness. The piecewise-power function plotted in red line is used to model the exposure time given the average of a photometrically normalized image.

A.3 More on Doomer Dataset

In the full public release of Doomer dataset we will provide 3 main versions:

1. **RAW version.** Images from all cameras before any preprocessing.
2. **Single-camera version.** Pairs of a Main-camera photo and an HSI. The images are preprocessed and share the same FoV and spatial resolution.
3. **Multi-camera version.** Quadruples of Main-, Tele- and Wide-camera photos and HSI. The images are preprocessed and share the same FoV and spatial resolution.

Both the single- and multi-camera versions will also have two subversions of hyperspectral sampling interval: 3 nm or 10 nm. A short summary of each version provided in Tab. 6.

The preprocessing pipeline of RAW images consists of these steps: demosaicing, black current subtraction, flat field calibration and photometric normalization. For hyperspectral images, preprocessing pipeline includes: black current subtraction, flat

field calibration, radial distortion correction and photometric normalization. The last step involves only division by the exposure time (Specim IQ has no ISO setting) and band-wise division by the calibration divisor k .

Dataset version	Smartphone images	HSIs		FoV matching
		spectral range (step)		
RAW	Main, Tele, Wide	Original 400–1000 nm (3 nm)		–
1-camera	Preprocessed Main camera image	Preprocessed 400–730 nm (10 nm)	Preprocessed 400–730 nm (3 nm)	✓
3-camera	Preprocessed and concatenated Main, Tele, Wide images	Preprocessed 400–730 nm (10 nm)	Preprocessed 400–730 nm (3 nm)	✓

Table 6: Doomer Dataset versions

For all HSIs, we will provide a manually annotated binary mask that specifies the location of the gray ball. The reflectance spectrum of the gray ball, measured with the X-Rite spectrophotometer, will be included in the dataset. Also, we will expand it by adding more scenes and annotate each scene with tags depending on its contents.

Unlike previously published datasets, Doomer contains multiple real RGB images along with ground-truth HSI and illumination reference. This combination enables the exploration of various computational photography problems, such as:

1. *White point estimation* both in spectral and RGB forms.
2. *Illumination distribution estimation*. The need to estimate a distribution of illumination in a scene arises from the complexity of natural scenes. In such environments, a single global white point may be insufficient for accurate image processing and color correction [46].
3. *Color space transform*. Since there is a known white-point for each scene, it is possible to do precise chromatic adaptation and color signals for different cameras.
4. *Hyperspectral Reconstruction*. Reconstruction from single or multiple cameras. Reconstruction of different types of spectra — radiance or reflectance.

The data preprocessing pipeline was described in Sec. 4 and is briefly illustrated in Fig. 14.

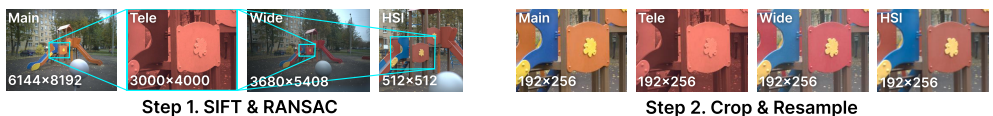


Figure 14: *Spatial preprocessing pipeline*. Left: geometric alignment of RGB views using SIFT + RANSAC for consistent cross-camera registration. Right: field-of-view normalization and resolution matching across RGB and hyperspectral modalities.

A.4 Comparison of alignment methods

We evaluate the impact of different image alignment strategies on the proposed Doomer dataset, with results summarized in Table 7. Additional global alignment based on homography, implemented via ASpanFormer [47], provides limited improvement, as it fails to handle parallax effects. We also try simply warping the inputs according to the computed optical flow, which is equivalent to applying 1×1 deformable convolution with identity features transform. It substantially improves performance by enabling dense, non-rigid correspondence. However, integrating optical flow into the proposed DCAM consistently yields further gains, demonstrating the advantage of task-aware features learning with respect to alignment. Among all variants, DCAM with PWC-Net achieves the best overall performance, further validating our choice of the optical flow network over the recent of Teed and Deng [48].

Alignment type	Alignment network	PSNR, dB \uparrow	SAM, $^\circ$ \downarrow	NSE, % \downarrow
None	None	30.76	4.41	9.62
Homography	AspanFormer [47]	30.44	4.29	9.44
Optical flow-only	PWC-Net [40]	30.99	4.10	8.71
	RAFT [48]	31.22	4.10	8.24
DCAM	PWC-Net [40]	31.46	3.91	8.35
	RAFT [48]	31.05	4.53	8.63

Table 7: Impact of different alignment technics on the overall reconstruction quality. Evaluated on the Doomer dataset. **Best** results are highlighted.